World Journal of Advanced Engineering Technology and Sciences
eISSN: 2582-8266
Cross Ref DOI: 10.30574/wjaets
Journal homepage: https://wjaets.com/

(RESEARCH ARTICLE)

Check for updates

Fabrication of a zinc-based coating with titanium dioxide on AM50 and AZ91 magnesium alloys

Aviva Fredj Elias [1], Yossi Elias [2], Harel Cohen [1] and Svetlana Lugovskoy [1,*]

[1] *Department of Chemical Engineering, Ariel University, Ariel, Kiryat Hamada, 40700, Israel.*
[2] *Department of Computer Science, Ariel University, Ariel, Kiryat Hamada, 40700, Israel.*

World Journal of Advanced Engineering Technology and Sciences, 2025, 16(01), 216-230

Publication history: Received on 31 May 2025; revised on 05 July 2025; accepted on 08 July 2025

Article DOI: https://doi.org/10.30574/wjaets.2025.16.1.1208

Abstract

This study investigated the formation of zinc coatings incorporated with titanium dioxide (TiO_2) on magnesium alloys designated as AM50 and AZ91. The coating process involved electrochemical zinc deposition, with and without concurrent electrophoresis of TiO_2 particles in the deposited flux. Various analytical techniques were employed, including scanning electron microscopy (SEM), energy dispersive spectroscopy (EDS), X-ray diffraction (XRD), and electrochemical methods. The resulting zinc-TiO_2 coating exhibited a titanium concentration approximately double that of the initial electrolyte. Additionally, an unexpected phase transition from rutile to anatase TiO_2 was observed at room temperature. Corrosion tests revealed that while the pure zinc-coated alloys exhibited higher corrosion rates compared to their uncoated counterparts, the inclusion of TiO_2 in the zinc coating slightly reduced this corrosion rate. The corrosion behavior of both the coated AM50 and AZ91 alloys differed from that of the uncoated alloys.

Keywords: Magnesium Alloys; Corrosion; Titanium Oxides; Zn Electrodeposition

1. Introduction

The field of orthopedic and dental implantology has seen significant advancements in recent years, with a growing interest in biodegradable materials that can provide temporary support during tissue healing and then gradually dissolve in the body. Among these materials, magnesium alloys have emerged as promising candidates, due to their unique combination of biocompatibility, biodegradability, and mechanical properties similar to natural bone [1]. In particular, two magnesium alloys, AM50 and AZ91, have garnered attention for their potential applications in implantology [2,3].

Magnesium is an essential element in the human body, playing crucial roles in various physiological processes, including bone metabolism and tissue repair [4]. This inherent biocompatibility, coupled with the ability to tailor the degradation rates of magnesium alloys, presents an opportunity to develop implants that can gradually transfer loads to healing tissue, potentially improving the osseointegration process [5-7]. The Young's modulus of magnesium alloys (40-45 GPa) closely resembles that of natural bone (10-40 GPa), which can help minimize stress shielding effects commonly observed with conventional metallic implants such as titanium (110 GPa) or stainless steel (200 GPa) [5-9].

AM50 and AZ91 alloys, containing aluminum and manganese or aluminum and zinc, respectively, offer distinct advantages in terms of mechanical strength and corrosion resistance [6]. They show a particularly appealing promise for surgical implants such as pins, brackets, staples, and bone-fixing screws, which can dissolve during healing [8] and thus eliminate the need for removal surgery. Magnesium and its compounds are biocompatible and may even enhance bone formation [8]. However, the complex interplay between these alloys and the biological environment necessitates

* Corresponding author: Svetlana Lugovskoy

a thorough investigation of their biocompatibility and osseointegration properties [7]. Understanding these interactions is crucial for optimizing implant design and ensuring safe and effective clinical applications.

Two main challenges currently hinder widespread adoption of these implant materials: uncontrolled biodegradation rates, and suboptimal osseointegration. While magnesium shows better osseointegration than titanium, the metal-bone tissue interface remains problematic [9-16]. The rapid initial corrosion of magnesium alloys in physiological environments can lead to hydrogen gas evolution, local alkalinization, and premature loss of mechanical integrity before sufficient tissue healing occurs [17-19]. These factors necessitate innovative approaches to modulate the degradation kinetics while enhancing bioactivity.

This study proposes a method to accelerate magnesium alloy dissolution by applying a more cathodic metal coating. To improve osseointegration, titanium dioxide (TiO_2) particles were incorporated into the coating. TiO_2 has demonstrated bactericidal properties and enhanced bone tissue integration [16-18], but its impact on magnesium substrate corrosion requires investigation. The rationale behind this approach lies in the galvanic coupling effect between the coating and substrate, which can be leveraged to control degradation rates through careful selection of coating materials and thicknesses [19, 20].

Recent studies have shown that surface modifications and coatings can significantly influence the biological response to magnesium implants by altering protein adsorption, cell adhesion, and subsequent tissue integration [21-23]. Therefore, our comprehensive investigation includes not only corrosion behavior analysis but also evaluation of cytotoxicity, cell adhesion, proliferation, and differentiation to provide insights into the biocompatibility and potential clinical efficacy of these systems [24, 25].

By addressing these critical aspects of biodegradable magnesium alloys, this research contributes to the ongoing efforts to develop next-generation implant materials that can overcome the limitations of current options and potentially revolutionize treatment approaches in orthopedic and dental implantology [23-25]. The findings from this study may guide future design strategies for biodegradable implants with tailored degradation profiles and enhanced osseointegration capabilities.

Our research compared the morphology and corrosion properties of three systems: uncoated AM50 and AZ91 magnesium alloys, zinc-coated alloys, and zinc-coated alloys with impregnated TiO_2 particles. The selection of zinc as a coating material was motivated by its essential role in cellular functions, including protein synthesis, cell division, and DNA synthesis, as well as its relatively higher standard electrode potential compared to magnesium [25]. The incorporation of TiO_2 particles aims to create a multifunctional coating that combines controlled biodegradation with enhanced bioactivity and antimicrobial properties.

2. Materials and Methods

Rectangular 20x20x1 mm plates of AM50 and AZ91 alloys (China Royal Group Ltd., Tianjin, China) were ground with diamond paper #340, #500, #1200 and #2000, and then degreased in acetone in an ultrasonic bath and rinsed in distilled water. After drying, a current lead was attached to a specimen and the whole bunch was sealed by a polymer film so that only a 1 cm diameter round window (area 1 cm2) was available to further electrochemical treatment.

Zinc coating was produced in potentiation mode in a three-electrode cell under the potential of -1.3V vs. Ag| Ag Cl during 40 minutes.

The electrolyte contained 100 g/L $ZnSO_4$, 15 g CH_3COONa, 50 g/L $MgSO_4$, 200 mL/L glycerol the prepared zinc coating, along with 1 g/L micron-sized particles of TiO_2 rutile (Sigma Aldrich), and the electrolyte suspension was shaken for 72 hours.

The corrosion resistance was determined on a potentiated (Avium-n-Stat; Avium Technologies, Eindhoven, Netherlands) by linear polarization resistance (LPR) and Tafel slope extrapolation (TSE) using a three-electrode cell, where an Ag| Ag Cl electrode served as the reference electrode, and a platinum wire was the counter electrode. All the corrosion tests were performed in 3 wt. % NaCl solution.

Tafel polarization measurements were conducted within a potential range of -0.250 V to +0.250 V (vs. OpenShift Container Platform OCP) with a step potential of 0.34 mV and a scan rate of 1 mV/s. All measurements were performed on specimens with a standardized surface area of 1 cm^2. To ensure statistical reliability, each sample was subjected to triplicate measurements, and the reported results represent the statistical mean of these measurements.

Linear polarization resistance (LPR) measurements were performed within a narrow potential window of -0.010 V to +0.010 V (vs. OCP), employing a step potential of 0.34 mV and a scan rate of 1 mV/s. As with the LPR analysis, all specimens had a uniform surface area of 1 cm^2. Statistical robustness was ensured by conducting triplicate measurements for each sample, with the presented data representing the statistical average of these measurements.

The surface morphology and elemental composition were characterized by scanning electron microscope (SEM; Triglid TM TESCAN MAIA3) equipped with an energy dispersive spectroscopy (EDS) analyzer (Aste, Oxford, UK). The Phi-Rho-Z (PROZA) correction method was used for quantization.

An X-ray diffractometer (Pert Pro; PAN atypical B.V., Eindhoven, Netherlands) with Cu Kα radiation (λ = 0.154 nm) was used with full pattern identification by the Pert High Score-Plus software package (Analytical B.V.; version 2.2e/ 2.2.5). Materials identification and analysis were performed using the Powder Diffraction Filet (PDF®; ICDD, USA; v.2, 2009). Phase analysis identification was performed at 40 kV and 40 mA. The XRD patterns were recorded via grazing incidence x-ray diffraction (GIXD) with the geometry α = 1◦ and 5◦ in the 20–80◦ range (step size was 0.05◦ and the time per step was 2 s).

When calculating the scattering of titanium particles, the coding which helps us understand it quantitatively is briefly presented here. In the first step, a mapping analysis was performed using EDS analysis. After receiving the image, a cut was made to a perfect square shape that can be cut into smaller perfect squares. In each small square, the number of particles was counted. Since the size of the squares is fixed, the density of the points is the critical part with which we can examine the scattering. Figure 1 shows the simulation for the cutting and point-counting process. After checking the return density in each subarea, a standard deviation test was performed to estimate the uniformity of the scattering.

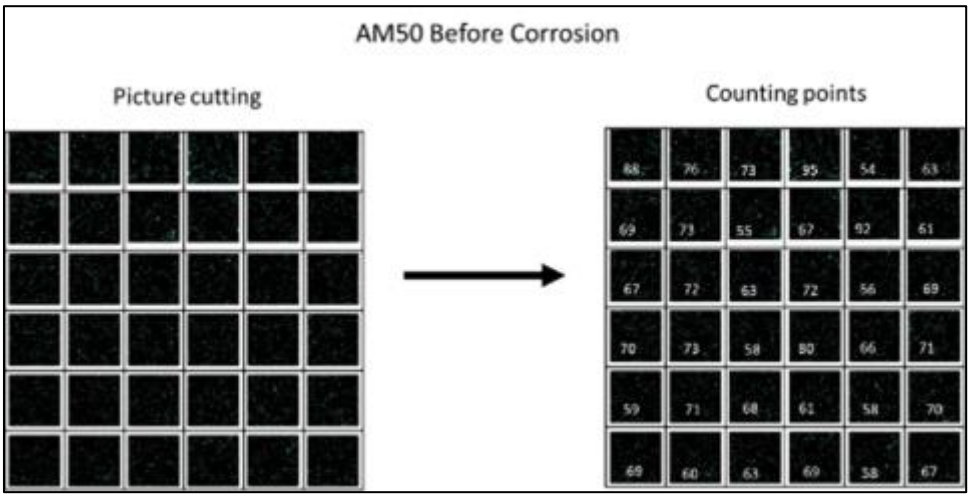

Figure 1 Simulation for scattering of titanium particles, the point-counting and cutting process

2.1. Pseudocode

- Upload an image to Python as a jpg file.
- Crop the image to size n*n.
- Crop the image into K images.
- Count the dots drawn in each image of size n*n.
- Create a graph in which the number of dots in each image is recorded.
- Calculate the standard deviation of the number of dots and the overall average of the dots.
- Analysis.

Due to the purely descriptive nature of this study, no statistical model involving concepts such as "p-value" or "null hypothesis" could be formulated. The only statistical analysis performed was the calculation of the dispersion of measurement results, determined using the mean squared deviations from the average for each series of repeated measurements.

3. Results and Discussion

The formation of a zinc-titanium dioxide layer in an electrolyte involves the following processes: (a) reduction of zinc from the electrolyte solution (b) adsorption of TiO_2 particles onto the sample surface. The critical aspect is the balance between the rates of these two competing processes.

Since the rate of the first process is quite high, it was important to select the concentration of TiO_2 and the particle size to ensure the transfer and deposition of these particles on the sample.

- $Zn^{2+} \rightarrow Zn^0$
- $[Zn^{2+} - TiO_2] \rightarrow [Zn^0 - TiO_2]$ - transport of titanium dioxide particles to the sample surface by zinc cations

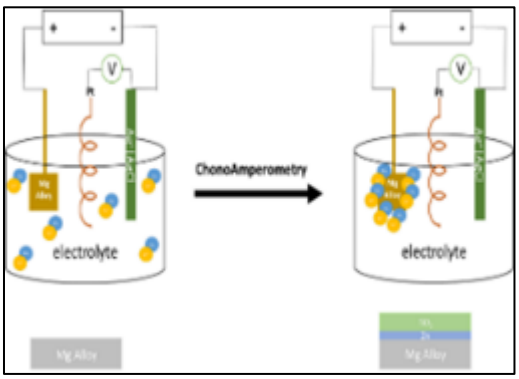

Figure 2 Scheme illustrating the process of zinc coating formation on a sample in the presence of titanium dioxide particles

The coatings produced on the surface of AM50 are shown in Figure 3. As seen in Figure 3b, the zinc formed a cracked, continuous layer. The cracks were obviously the result of the heteroepitaxial growth of zinc (HCP lattice, d = 0.266 nm) on the magnesium substrate (HCP lattice, d = 0.320 nm) [18].

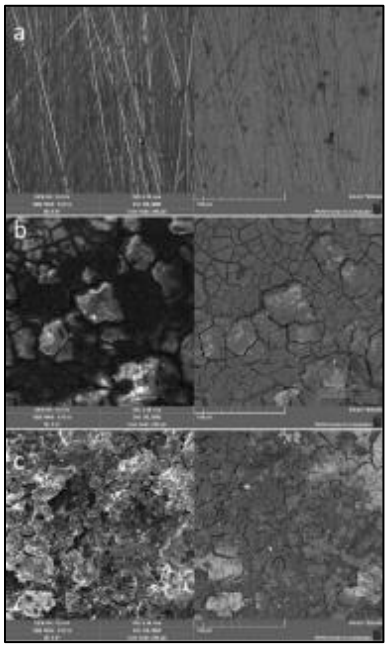

Figure 3 Secondary electron (left) and back-scattered electron (right) SEM images of the surfaces of (a) uncoated AM50 alloy, (b) zinc-coated AM50 and (c) AM50 coated with zinc containing TiO_2. Magnification x1000. Dark spots are inclusions of diamond powder remaining after surface grinding

When titanium dioxide was present in the coating (Figure 3c), the surface appearance changed unexpectedly: TiO_2 did not form a distinct surface phase, which would have shown as darker spots in a BSE image. (The atomic mass of titanium is 48 amu, while that of zinc is 65 amu.) Instead, the granular structure of the zinc containing TiO_2 (Figure 3c) was considerably finer than that of pure zinc (Figure 3b).

SEM analysis of the electrodeposited coatings on AZ91 substrate is presented in Figure 4. The zinc coating morphology, depicted in Figure 4b, exhibited a continuous layer characterized by distinctive crack formation, analogous to observations made on the AM50 substrate. The incorporation of TiO_2 into the coating structure (Figure 4c) resulted in notable grain refinement. Back-scattered electron (BSE) imaging revealed the absence of distinct TiO_2 surface phases, which would manifest as regions of lower contrast due to the atomic mass differential between titanium (48 amu) and zinc (65 amu).

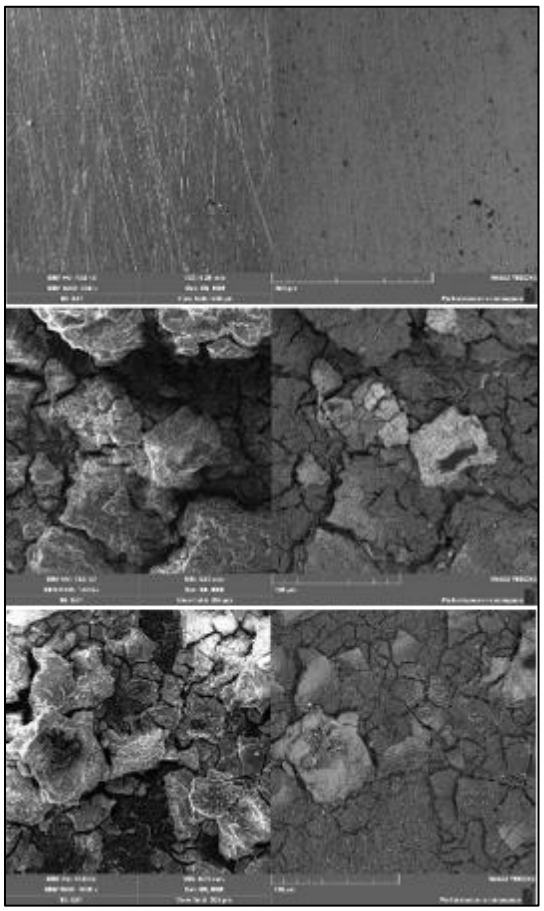

Figure 4 Secondary electron (left) and back-scattered electron (right) SEM images of the surfaces of (a) uncoated AZ91 alloy, (b) zinc-coated AZ91 and (c) AZ91 coated with zinc containing TiO_2. Magnification x1000

The mass ratio of zinc sulfate to titanium dioxide in the electrolyte was $ZnSO4:TiO_2$ = 100:1; the corresponding nominal atomic ratio ZN:TI = 50:1. According to EDS spectrum and EDS mapping (Figures 5, 6), the observed ratio was ZN:TI = 24:1 in AM 50 and ZN: TI = 46:1 in AZ91. This confirmed that the efficacy of the co-deposition of TiO_2 powder in the flux of zinc ions was very high; the surface concentration of titanium in zinc was twice as high as its initial concentration in the electrolyte. As is seen from the Ti mapping image in Figures 5 and 6, titanium was very evenly distributed on the surface.

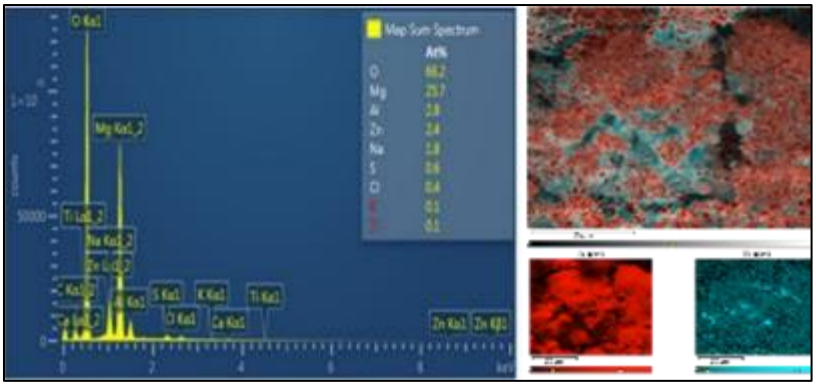

Figure 5 On the left: EDS spectrum and atomic percentage of elements on the surface of AM50 coated with Zn containing TiO_2. On the right: an EDS mapping image of Ti distribution on the surface of the specimen

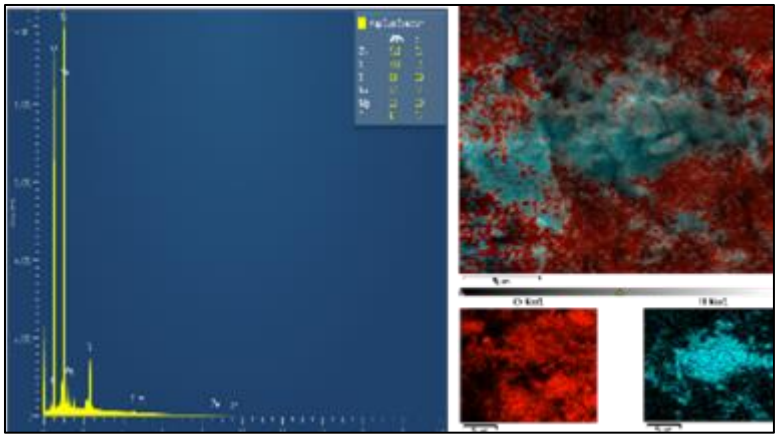

Figure 6 On the left: EDS analysis of zinc-coated AZ91 magnesium alloy containing titanium dioxide. The right side: an EDS elemental map specifically showing how titanium was distributed across the specimen surface

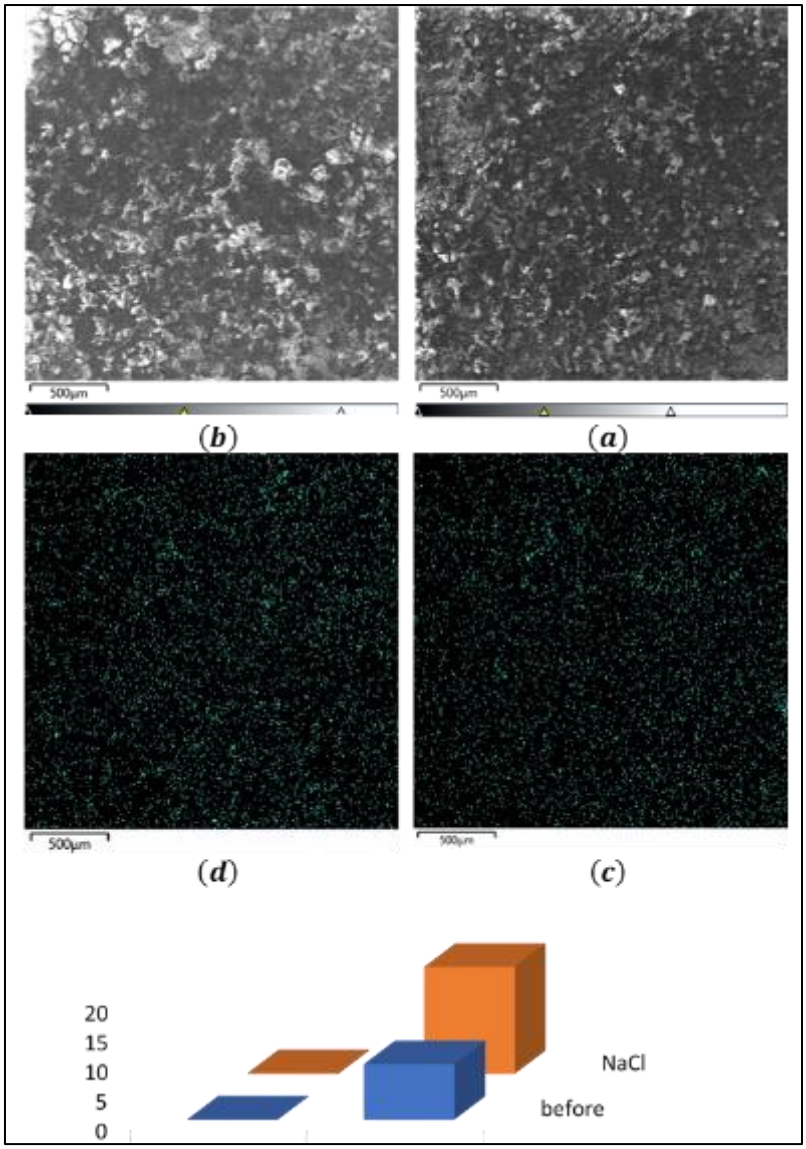

	Corrosion [mm/year]	Standard deviation
before	0.07	9.40
NaCl	0.19	18.15

Figure 7 SEM images. AM50 after coating. SEM image and scattering of titanium particles. (a) and (c) before corrosion, (b) and (d) after corrosion in NaCl 3% (WT). Comparison of dispersion and corrosion rate

Figure 7 presents comparative SEM micrographs obtained before and after corrosion testing. While visual inspection at fixed magnification reveals no substantial morphological differences, the scattered signal intensity exhibits notable enhancement across all observation distances. To quantitatively characterize the TiO_2 scattering behavior, we analyzed the spatial distribution of reflected light intensity per unit area using EDS mapping. The resulting high-resolution images were processed to account for potential artifacts arising from signal interference, including overlapping effects and background noise. Statistical analysis was performed using Python-based image processing algorithms to isolate and quantify reflection intensities. The standard deviation of these measurements was calculated to enable quantitative comparison of the previously qualitative observations, with results summarized in Table 1.

Table 1 Python results table – for AM50 and AZ91 alloys before corrosion measurement, after corrosion measurement in 3%(WT) NaCl solution

	AM50-before	**AM50- after**	**AZ91- before**	**AZ91- after**
Average of the dispersion	68.22	104.03	65.58	98.28
Standard deviation	9.40	14.22	8.29	10.03
The amount of titanium dioxide particles on the selected surface in %	86.22%	86.33%	87.36%	89.79%

In the XRD spectra of AM50 and AZ91, the peaks of the XRD pattern were typical for these two alloys before corrosion. The appearance of the Mg and Zn oxide phase (peak growth) after corrosion testing (red spectrum in Figs. 7 and 9) showed an obvious oxidation process of Mg and Zn in the surface layer of the coating. Along with this, the rutile phase remained unchanged, both quantitatively and qualitatively, before and after corrosion testing.

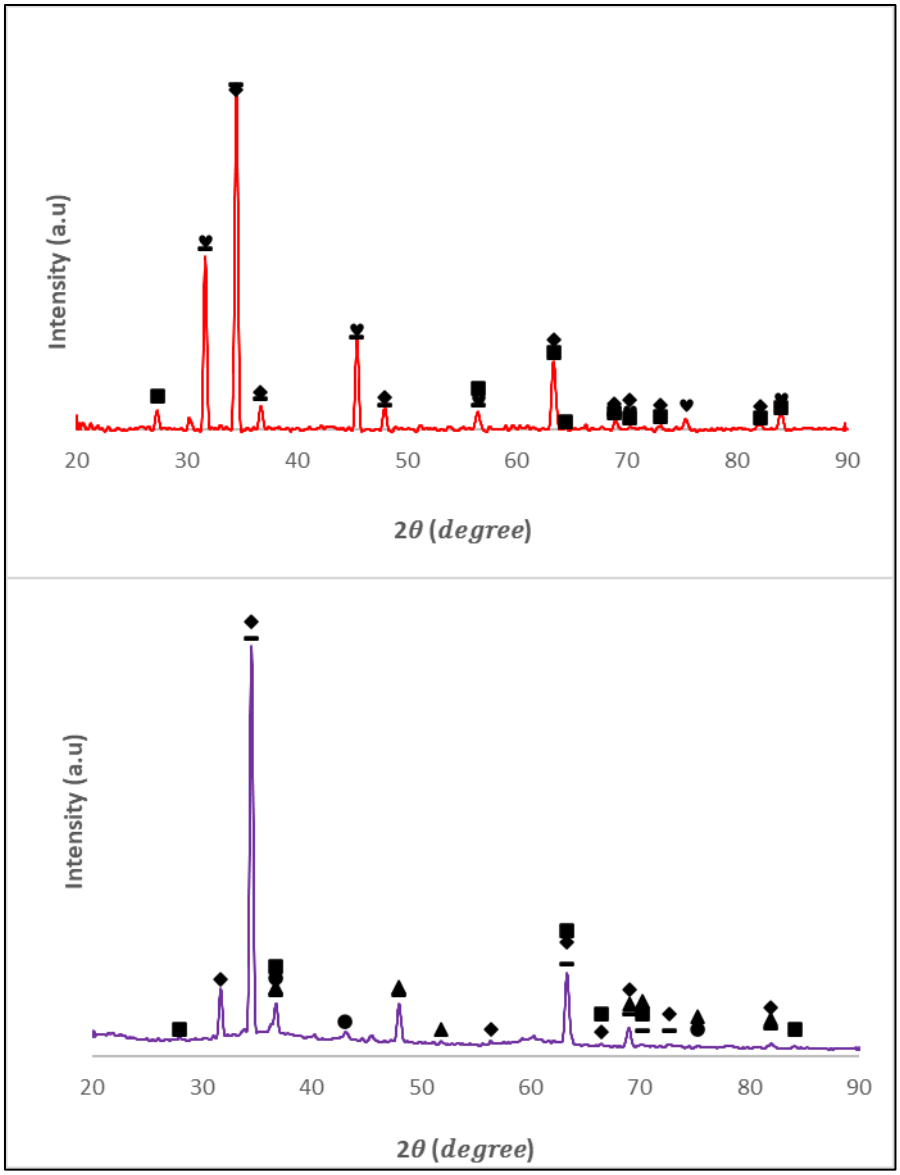

Figure 8 XRD patterns of AM50 coated with Zn and TiO_2 (top), and uncoated AM50 alloy (bottom)

	AM50+Zn+TiO_2 before	▬	Mg	◆	ZnO
		✚	Zn	■	TiO_2 Rutile
	AM50+Zn+TiO_2 in NaCl	●	MgO	❤	$Al_{2.4}MgO_{0.39}O_4$

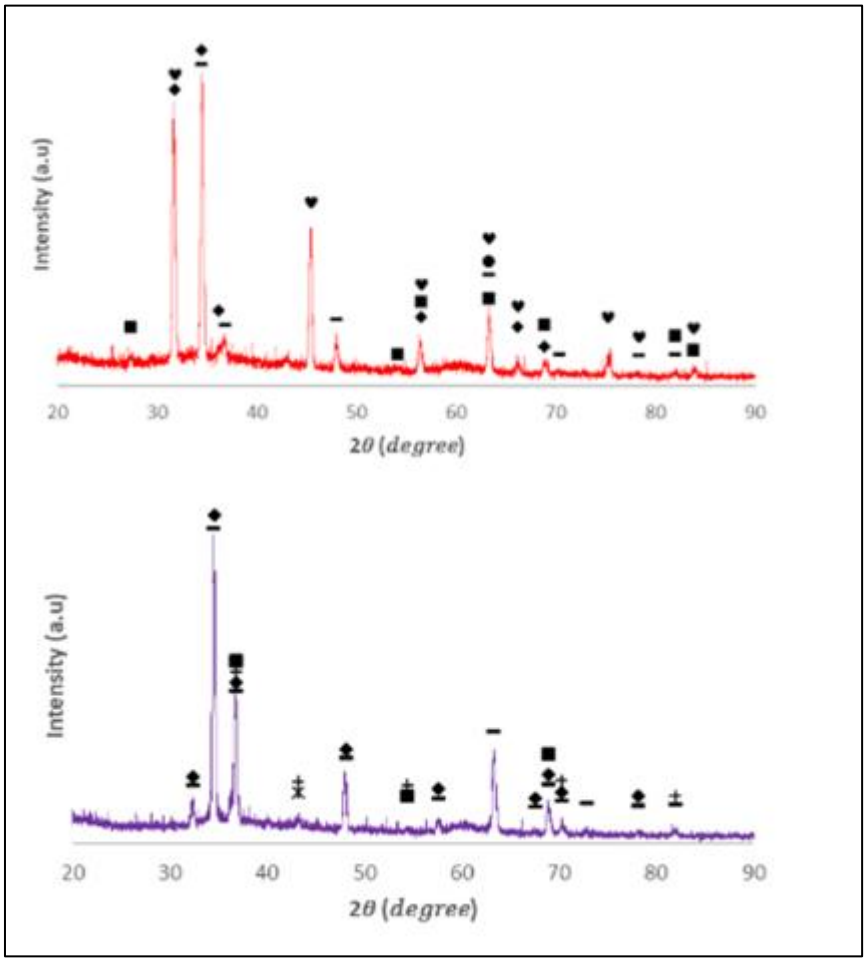

Figure 9 XRD patterns of AZ91 coated with Zn and TiO_2 (top), and uncoated AZ91 alloy (bottom)

	AZ91 before corrosion	▬	Mg	◆	ZnO
		✚	Zn	■	TiO_2 Rutile
	AZ91 in NaCl	●	MgO	❤	$Al_{2.4}MgO_{0.39}O_4$

Polarization curves mapping the corrosion of the alloy AM50 in 3 wt. % NaCl at room temperature are shown in Figure 10, and the corresponding corrosion currents and potentials are given in Table 2.

The corrosion potentials (Ecor), corrosion current densities (Icor), and slopes of the linear sections corresponding to the anodic and cathodic processes (βa and βc) were assessed from the appropriate polarization curves in Tafel coordinates. The polarization resistance values (Rp) were then calculated using the Stern-Geary equation [26].

$$R_p = \frac{\beta_a \times \beta_c}{2.3 \times i_{cor} \times (\beta_a + \beta_c)}$$

According to the obtained parameters (Ecorr, Icorr, βa, βc) and calculated polarization resistance (Rp)

Table 2 Corrosion potentials and currents measured by OpenShift Container Platform monitoring (OCP), Tafel slope extrapolation (Tafel) and linear polarization resistance (LPR) for AM50 alloy with and without coatings in 3 wt. % NaCl

	E_{cor}, V		i_{cor}, µA/cm²	
	OCP	**Tafel**	**Tafel**	**LPR**
AM50	- 1.551	- 1.511	15.7	24.4
AM50 + Zn	- 1.490	- 1.465	47	52
AM50 + Zn + TiO_2	- 1.540	- 1.465	36.8	45.5

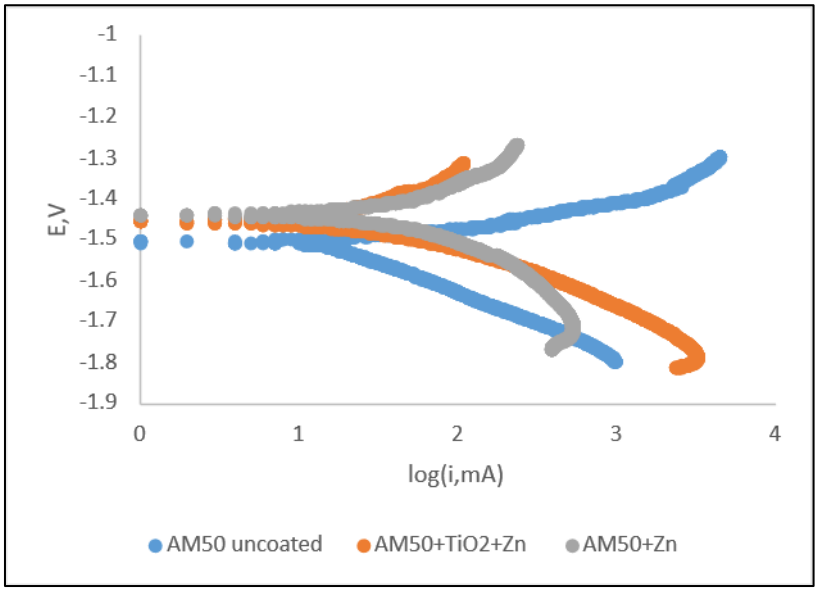

Figure 10 Polarization curves of AM50 alloy with and without coatings in 3 wt. % NaCl

As demonstrated in Figure 10, the application of a zinc coating resulted in a shift of the alloy toward more noble potentials. This behavior aligns with fundamental electrochemical principles, given that zinc exhibits a significantly higher standard electrode potential (Eo = -0.76V) compared to magnesium (Eo = -2.37V) [15]. This electrochemical nobility difference creates a galvanic coupling between the coating and substrate, establishing the theoretical basis for sacrificial protection of the magnesium alloy.

However, the experimental data revealed an interesting contradiction: The corrosion current densities for the zinc-coated specimens were observed to be two to three times greater than those measured for the uncoated AM50 alloy. While the zinc coating provided initial protective benefits through its sacrificial nature, once corrosion initiation occurred, the degradation process proceeded at a substantially accelerated rate compared to the uncoated magnesium alloy. This acceleration can be attributed to the galvanic coupling effect between zinc and magnesium, which, while providing cathodic protection, simultaneously increases the overall corrosion rate.

The polarization curves exhibited characteristic features typical of magnesium alloy corrosion behavior, with cathodic Tafel slopes consistently exceeding their anodic counterparts for all specimens (Figure 10). Both the uncoated and zinc-coated AM50 alloy demonstrated polarization curves characteristic of magnesium alloys under cathodic control [13,14]. However, a notable transition toward mixed control was observed when AM50 was coated with zinc, regardless of TiO_2 presence. This observation correlates well with the established theory regarding the corrosion mechanism of magnesium alloys in NaCl solutions, which posits that corrosion initiation occurs through the breakdown of the protective surface film by chloride anions [13]. The zinc coating serves as a partial barrier, moderating the access of chloride ions to the magnesium substrate, thereby altering the corrosion mechanism from predominantly cathodic to a more mixed control process. This transition in corrosion control mechanism provides strong evidence for the development of galvanic corrosion processes in the zinc-coated specimens.

LPR plots (Figure 11) demonstrated results similar to those of Tafel slope extrapolation (Table 2) and confirmed an accelerated corrosion after coating the magnesium alloy with zinc. The presence of TiO_2 particles in the zinc layer resulted in a corrosion current slightly smaller than for zinc only, but higher than for the uncoated AM50.

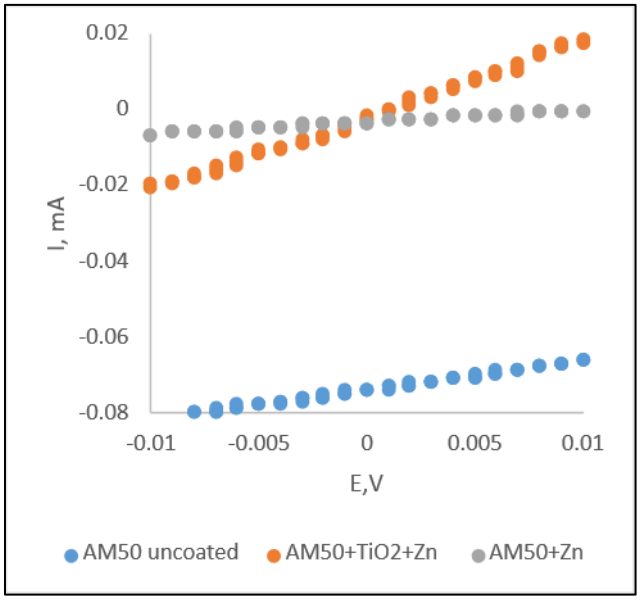

Figure 11 Linear polarization resistance (LPR) plots of AM50 alloy, with and without coatings, in 3 wt. % NaCl

The electrochemical behavior of the AZ91 alloy demonstrated distinctive characteristics that merit detailed examination. A notable shift toward noble potential was observed, aligning with previously established mechanistic frameworks for magnesium alloy corrosion. The corrosion current density measurements revealed substantial differences in degradation kinetics between coated and uncoated specimens [27]. Specifically, the uncoated AZ91 substrate exhibited corrosion current values approximately twice those of the zinc-TiO_2 coated samples, providing quantitative evidence for the protective efficacy of the composite coating system.

This enhanced corrosion resistance can be primarily attributed to the elevated aluminum content (mass %) in AZ91 compared to AM50 [28]. The increased aluminum concentration plays a crucial role through multiple mechanisms: first, by promoting the formation of a more stable protective oxide layer (Al_2O_3) that acts as a passive barrier [29]; second, by contributing to the ennoblement of the electrochemical potential through the formation of oxide phases (primarily Al2.4Mg00.39O4 oxide phase, the formation of which is visible in the XRD spectrum) [30]; and third, by modifying the microstructural characteristics of the alloy [31]. These combined effects result in a significant alteration of the system's overall corrosion behavior, particularly in terms of both initiation and propagation kinetics.

Analysis of the polarization curves (Figure 12) revealed a consistent pattern where cathodic Tafel slopes exceeded their anodic counterparts across all specimen configurations. This characteristic polarization behavior, indicative of cathodic control, aligns with the typical electrochemical responses documented for magnesium alloys. The preservation of this cathodic control mechanism in both uncoated and zinc-electrodeposited AZ91 substrates suggests that while the composite coating modifies the corrosion rates, it does not fundamentally alter the underlying electrochemical reaction mechanisms. This maintenance of cathodic control implies that the rate-determining step in the corrosion process remains associated with the cathodic partial reaction, specifically the reduction of water and evolution of hydrogen, which is characteristic of magnesium alloy corrosion in aqueous environments.

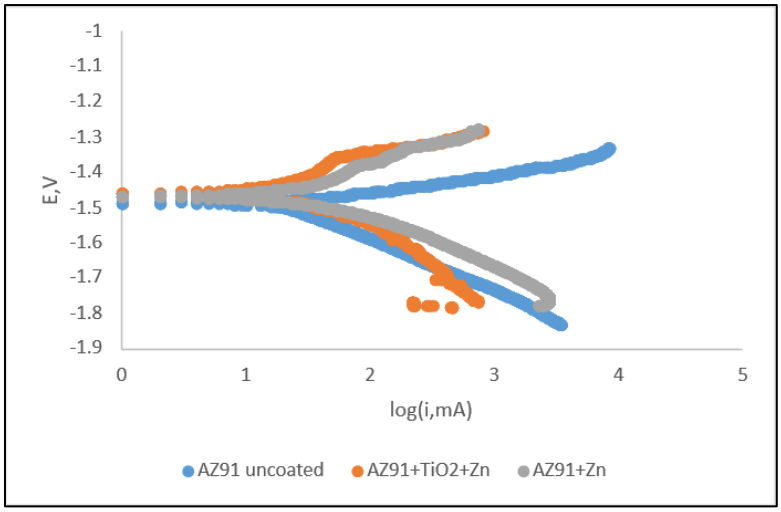

Figure 12 Polarization curves of AZ91 alloy, with and without coatings, in 3 wt. % NaCl

LPR measurements (Figure 13) corroborated the findings obtained through Tafel slope extrapolation analysis (Table 3), validating the observed reduction in corrosion kinetics following zinc electrodeposition on the magnesium alloy substrate. Furthermore, the incorporation of TiO_2 particles into the zinc matrix resulted in diminished corrosion current densities, compared to both pure zinc coatings and uncoated AM50 specimens.

Table 3 Corrosion potentials and currents measured by OCP monitoring (OCP), Tafel slope extrapolation (Tafel) and linear polarization resistance (LPR) for AZ91 alloy, with and without coatings, in 3 wt. % NaCl

	E_{cor}, V		i_{cor}, µA/cm²	
	OCP	**Tafel**	**Tafel**	**LPR**
AZ91	- 1.569	-1.511	67.76	66.72
AZ91 + Zn	- 1.612	- 1.505	35.72	58.67
AZ91 + Zn + TiO_2	- 1.596	- 1.469	29.09	64.83

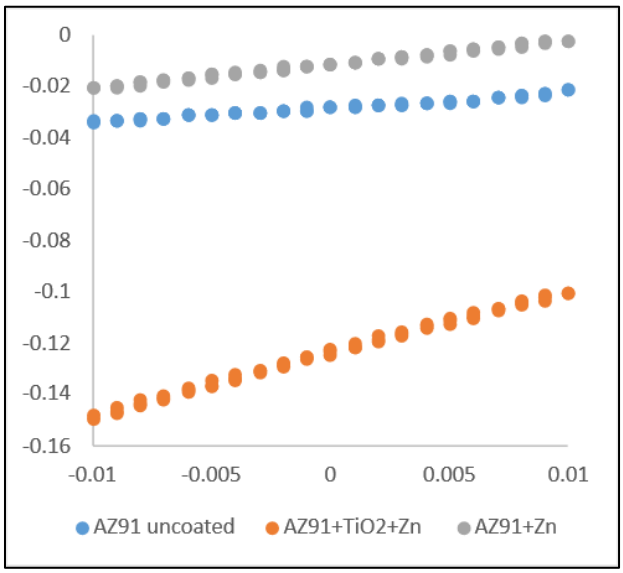

Figure 13 Linear polarization resistance (LPR) plots of AZ91 alloy, with and without coatings, in 3 wt. % NaCl

Magnesium dissolution in aqueous environments typically occurs through an electrochemical reaction with water, resulting in the formation of magnesium hydroxide and hydrogen gas. Consequently, magnesium corrosion tends to be relatively unaffected by oxygen concentration, [32-34] although oxygen presence plays a significant role in atmospheric corrosion.[34] In aqueous environments, corrosion often involves micro-galvanic coupling between cathodic and anodic regions.[33] The overall corrosion reaction can be described as follows:[32]

$$Mg + 2H_2O \rightarrow Mg(OH)_2 + H_2 \quad \ldots\ldots\ldots (1)$$

This overall reaction may be expressed as the sum of the following partial reactions

$$Mg^0 \rightarrow Mg^{2+} + 2e^- \text{ (anodic reaction) } \ldots\ldots\ldots\ldots (2)$$

$$2H_2O + 2e^- \rightarrow H_2 + 2OH^- \text{ (cathodic reaction) } \ldots\ldots\ldots\ldots (3)$$

$$Mg^{2+} + 2OH^- \rightarrow Mg(OH)_2 \text{ (product formation) } \ldots\ldots\ldots (4)$$

However, given that we are dealing with a sandwich coating of AM50 and AZ91, we can assume a mixed corrosion mechanism involving the anodic reactions as follows

$$Zn^0 \rightarrow Zn^{2+} + 2e^-$$

$$Mg^0 \rightarrow Mg^{2+} + 2e^-$$

The second reaction may occur if the coating is non-uniform or if all the zinc from the surface layer has reacted. However, based on our XRD results, we have identified oxide forms of metals present on the surface. This indicates that magnesium exists in the surface layer in very limited quantities, as we do not observe the formation of $Mg(OH)_2$; instead, we detect the presence of zinc oxide and magnesium oxide phases.

The enhancement in corrosion resistance can be attributed to several factors related to the refined granular morphology induced by TiO_2 incorporation.

The refined microstructure leads to a more uniform distribution of the coating, which can reduce the likelihood of localized corrosion sites. This uniformity helps in minimizing the formation of micro-galvanic cells that can accelerate corrosion processes. The presence of TiO_2 not only influences the morphology but may also enhance the barrier properties of the zinc coating, effectively protecting the underlying magnesium alloys from corrosive environments.

The unique characteristics of TiO_2, such as its ability to form stable oxides and its interaction with the zinc matrix, contribute significantly to the observed outcomes.

In conclusion, the incorporation of TiO_2 not only refines the morphology of the zinc coatings but also enhances their protective characteristics, ultimately leading to improved corrosion resistance in the AZ91 alloy.

4. Conclusion

The incorporation of TiO_2 particles into zinc electrodeposits on AM50 and AZ91 magnesium alloys demonstrated remarkable efficiency, with titanium concentrations in the coating exceeding that of the initial electrolyte suspension. Microstructural analysis revealed that TiO_2-modified zinc coatings exhibited refined granular morphology, compared to pure zinc deposits.

Electrochemical characterization revealed substrate-dependent corrosion behavior. For AM50, the continuous zinc coating initially provided corrosion resistance; however, once initiated, the corrosion rate accelerated beyond that of the uncoated substrate. Conversely, AZ91 exhibited enhanced corrosion resistance with zinc coating, which was further improved by TiO_2 incorporation. Although the TiO_2 addition marginally decreased corrosion rates in zinc coatings for both alloys, the AM50 substrate maintained higher degradation rates, compared to its uncoated counterpart.

The surface concentration of titanium dioxide particles showed high values for both alloy samples, as quantified in Table 1. The particle density remained almost constant between the initial state after deposition and subsequent corrosion exposure, suggesting a uniform spatial distribution of TiO_2 particles over the substrate surface.

The corrosion mechanism analysis indicated a transition from localized chloride attack on uncoated alloys to predominantly galvanic corrosion in zinc-coated specimens. This modification of the degradation mechanism could enable tailored corrosion rates, which is particularly beneficial for AZ91. Given that AM50 exhibited accelerated dissolution, this property could be advantageously applied in the development of biodegradable magnesium implants where controlled degradation rates are crucial for prosthetic applications.

Compliance with ethical standards

Acknowledgments

We would like to express our sincere gratitude to Dr. Tamara Brider for SEM images, Dr. A. Kossenko for XRD analysis.

Disclosure of conflict of interest

The authors declare no conflict of interest.

References

[1] Witte, F. The history of biodegradable magnesium implants: A review. Acta Biomaterialia 2010, 6(5), 1680-1692. https://doi.org/10.1016/j.actbio.2010.02.028.

[2] Gu, X.N.; Zheng, Y.F. A review on magnesium alloys as biodegradable materials. Front. Mater. Sci. China 2010, 4, 111–115.

[3] https://doi.org/10.1007/s11706-010-0024-1

[4] Song, G. Control of biodegradation of biocompatible magnesium alloys. Corros. Sci. 2007, 49(4), 1696-1701.

[5] Staiger, M.P.; Pietak, A.M.; Huadmai, J.; Dias, G. Magnesium and its alloys as orthopedic biomaterials: A review. Biomaterials 2006, 27(9), 1728-1734.

[6] Zheng, Y.F.; Gu, X.N.; Witte, F. Biodegradable metals. Mat. Sci. Eng: R 2014, 77, 1-34.

[7] Agarwal, S.; Curtin, J.; Duffy, B.; Jaiswal, S. Biodegradable magnesium alloys for orthopaedic applications: A review on corrosion, biocompatibility and surface modifications. Mat. Sci. Eng: C 2016, 68, 948-963.

[8] Kirkland, N.T.; Birbilis, N.; Staiger, M.P. Assessing the corrosion of biodegradable magnesium implants: A critical review of current methodologies and their limitations. Acta Biomater. 2012 8(3), 925-936.

[9] Galli, S.; Stocchero, M.; Andersson, M.; Karlsson, J.; He, W.; Lilin, T.; Wennerberg, A.; Jimbo, R. The effect of magnesium on early osseointegration in osteoporotic bone: A histological and gene expression investigation. Osteoporos. Int. 2017, 28(7), 2195–2205.

[10] Castellani, C.; Lindtner, R.A.; Hausbrandt, P.; Tschegg, E.; Stanzl-Tschegg, S.E.; Zanoni, G.; Beck, S.; Weinberg, A-M. Bone-implant interface strength and osseointegration: Biodegradable magnesium alloy versus standard titanium control. Acta Biomater. 2011, 7(1), 432–440,.

[11] Radha, R.; Sreekanth, D. Insight of magnesium alloys and composites for orthopedic implant applications – A review. J. Magnes. Alloy 2017, 5, 286–312,.

[12] Huynh V.; Ngo, N.K.; Golden, T.D. Surface activation and pretreatments for biocompatible metals and alloys used in biomedical applications. Int. J. Biomater. 2019, 2, 1-21.

[13] Negahban A.; Shamsi M.; Sedighi, M. Advances in the modification of magnesium-based biomaterials to address corrosion and corrosion-fatigue: A review of developments and prospects. J. Mater. Res. Technol. 2024, 30, 4064-4108. https://doi.org/10.1016/j.jmrt.2024.04.038.

[14] Pardo, A.; Merino, M.C.; Coy, A.E.; Arabal, R.; Viejo, F.; Matykina, E. Corrosion behaviour of magnesium/aluminium alloys in 3.5 wt.% NaCl. Corros. Sci. 2008, 50, 823–834.

[15] Liang, J.; Hu, L.; Hao, J. Preparation and characterization of oxide films containing crystalline TiO_2 on magnesium alloy by plasma electrolytic oxidation. Electrochim. Acta. 2007, 52, 4836–4840.

[16] Wang, P.; Liu, D-X.; Li, J-P.; Guo, Y-C.; Yang, Z. Growth process and corrosion resistance of micro-arc oxidation coating on Mg-Zn-Gd magnesium alloys. T. Nonferr. Metal. Soc. 2010, 20(11), 2198-2203. https://doi.org/10.1016/S1003-6326(09)60442-8.

[17] Nahum, E.Z.; Lugovskoy, S.; Lugovskoy, A.; Sobolev, A. Surface properties of Ti65Zr alloy modified with TiZr oxide and hydroxyapatite. Nanomaterials-Basel 2024, 14(1), 15; https://doi.org/10.3390/nano14010015

[18] Jäger, M.; Jennissen, H.P.; Dittrich, F.; Fischer, A.; Köhling, H.L. Antimicrobial and osseointegration properties of nanostructured titanium orthopaedic implants. Nanomaterials-Basel 2017, 10(11), 1–28.

[19] Khan, A.R.; Grewal, N.S.; Zhou, C.; Yuan, K.; Zhang, H-J.; Jun, Z. Recent advances in biodegradable metals for implant applications: Exploring in vivo and in vitro responses. Results Eng. 2023, 20, 101526. https://doi.org/10.1016/j.rineng.2023.101526.

[20] Tsakiris V., Tardei C., Clicinschi F.M. Biodegradable Mg Alloys for Orthopedic Implants – A Review J. Magn. Alloys. 2021, 9, 1884–90.

[21] Seitz J-M., Eifler R., Bach Fr-W., Maier H J. Magnesium degradation products: effects on tissue and human metabolism. J Biomed Mater Res A. 2014, 102(10), 3744-53. DOI: 10.1002/jbm.a.35023

[22] Fajardo S., García-Galvan F.R., Barranco V., Galvan Ju. C and S.F.Batlle. A Critical Review of the Application of Electrochemical Techniques for Studying corrosion of Mg and Mg Alloys: Opportunities and Challenges. DOI: 10.5772/intechopen. Magnesium Alloys - Selected Issue Edited by Tomasz Tański, Wojciech Borek and Mariusz Król.

[23] Yun YH, Dong ZY, Lee N, Liu YJ, Xue DC, Guo XF, et al. Revolutionizing biodegradable metals. Mater Today. 2009, 12(22), –32.10.1016/S1369-7021(09)70273-1

[24] Kirkland NT, Birbilis N, Staiger MP. Assessing the corrosion of biodegradable magnesium implants: a critical review of current methodologies and their limitations. Acta Biomater, 2012, 8:925–36.10.1016/j.actbio.2011.11.014

[25] Dewei Zhao, Frank Witte, Faqiang Lu, Jiali Wang, Junlei Li, Ling Qin. Current status on clinical applications of magnesium-based orthopaedic implants: A review from clinical translational perspective. Biomaterials, 2017, 112, 287-302, https://doi.org/10.1016/j.biomaterials.2016.10.017.

[26] Moran Wang and Ning Pan. Predictions of effective physical properties of complex multiphase materials. Materials Science and Engineering: R: Reports. 2008, 63(1), 1-30, https://doi.org/10.1016/j.mser.2008.07.001

[27] Stern, M.; Geaby, A.L. Electrochemical Polarization. J. Electrochem. Soc. 1957, 104, 56–63.

[28] Arrabal, R.; Matykina, E.; Pardo, A.; Merino, M.C.; Paucar, K.; Mohedano, M.; Casajús, P. Corrosion behaviour of AZ91D and AM50 magnesium alloys with Nd and Gd additions in humid environments. Corros. Sci. 2012, 55, 351-362. https://doi.org/10.1016/j.corsci.2011.10.038.

[29] Song, Guang-Ling & Atrens, Andrej. Understanding Magnesium Corrosion—A Framework for Improved Alloy Performance. Advanced Engineering Materials. 2003, 5(12), 837-858.

[30] Liu, M; Schlesinger, M. Corrosion of magnesium and its alloys. Corrosion Science. 2009, 51(8), 1733-1737.

[31] Cao F. et al. Corrosion of ultra-high-purity Mg in 3.5% NaCl solution saturated with Mg(OH)2. Corrosion Science, 2013, 75, 78–99

[32] Milz M. P.; Wirtz A.; Abdulgader M.; Kalenborn A.; Biermann D.; Tillmann W. and Frank Walther. Corrosion Fatigue Behavior of Twin Wire Arc Sprayed and Machine Hammer Peened ZnAl4 Coatings on S355 J2C + C Substrate. Corros. Mater. Degrad. 2022, 3(1), 127-141; https://doi.org/10.3390/cmd3010007

[33] Makar G. L.; Kruger J.; Corrosion of magnesium. Int. Mater. Rev. 1993, 38(3), 138.

[34] Esmaily M.; Svensson J.E.; Fajardo S.; Birbilis N.; Frankel G.S.; Virtanen S.; Arrabal R.; Thomas S.; Johansson L.G. Fundamentals and advances in magnesium alloy corrosion. Progress in Materials Science. 2017, 89, 92-193. https://doi.org/10.1016/j.pmatsci.2017.04.011

[35] Revie R. Winston.; Uhlig Herbert H. Corrosion and Corrosion Control: An Introduction to Corrosion Science and Engineering. Print ISBN:9780471732792 |Online ISBN:9780470277270. DOI:10.1002/9780470277270